

Supplementary Information

**A double perovskite oxygen electrode in Zr-rich proton conducting ceramic cells for
efficient electricity generation and hydrogen production**

Haoyu Zheng,^{*ab} Matthias Riegraf,^a Noriko Sata^a and Rémi Costa^{*a}

^a Institute of Engineering Thermodynamics, German Aerospace Center (DLR),
Pfaffenwaldring 38-40, 70569 Stuttgart, Germany

^b Institute for Building Energetics, Thermotechnology and Energy Storage (IGTE), University
of Stuttgart. Pfaffenwaldring 31, 70569 Stuttgart, Germany

E-mail: zhenghaoyu01@gmail.com; remi.costa@dlr.de

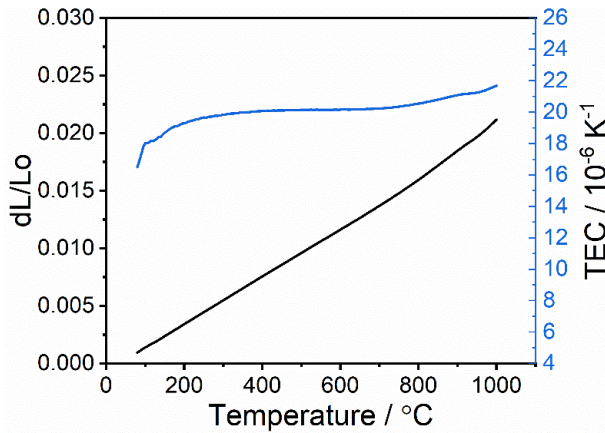


Figure S1. Thermal expansion behavior of BGLC587 from 80 °C to 1000 C in air.

Table S1. Comparison of BGLC587-BZCY541 oxygen electrode PCCs in fuel cell mode at 600 °C with perovskite-based oxygen electrode PCCs in previous studies.

Air electrode	electrolyte	Fuel electrode	PPD (mW cm^{-2})		Ref.
			600 °C	650 °C	
BGLC587-BZCY541	BZCY541	Ni-BZCY541	403	570	This work
$\text{LiNi}_{0.8}\text{Co}_{0.2}\text{O}_{2-\delta}$ $\text{BaZr}_{0.1}\text{Ce}_{0.7}\text{Y}_{0.2}\text{O}_{3-\delta}$	$\text{BaZr}_{0.1}\text{Ce}_{0.7}\text{Y}_{0.2}\text{O}_{3-\delta}$	$\text{Ni-BaZr}_{0.1}\text{Ce}_{0.7}\text{Y}_{0.2}\text{O}_{3-\delta}$		410	¹
$\text{SrSc}_{0.17}\text{Nb}_{0.025}\text{Co}_{0.8}\text{O}_{3-\delta}$	$\text{BaZr}_{0.1}\text{Ce}_{0.7}\text{Y}_{0.2}\text{O}_{3-\delta}$	$\text{Ni-BaZr}_{0.1}\text{Ce}_{0.7}\text{Y}_{0.2}\text{O}_{3-\delta}$	~260	~360	²
$\text{PrBa}_{0.5}\text{Sr}_{0.5}\text{Co}_2\text{O}_{5+\delta}-\text{BaZr}_{0.1}\text{Ce}_{0.7}\text{Y}_{0.2}\text{O}_{3-\delta}$	$\text{BaZr}_{0.1}\text{Ce}_{0.7}\text{Y}_{0.2}\text{O}_{3-\delta}$	$\text{Ni-BaZr}_{0.1}\text{Ce}_{0.7}\text{Y}_{0.2}\text{O}_{3-\delta}$	274	395	³
$\text{Ba}_{0.5}\text{Sr}_{0.5}\text{Co}_{0.8}\text{Fe}_{0.2}\text{O}_{3-\delta}$	$\text{BaCe}_{0.8}\text{Y}_{0.2}\text{O}_{3-\delta}$	$\text{Ni-BaCe}_{0.8}\text{Y}_{0.2}\text{O}_{3-\delta}$	~280	~400	⁴
$\text{Ba}_{0.5}\text{Sr}_{0.5}\text{Co}_{0.8}\text{Fe}_{0.2}\text{O}_{3-\delta}$	$\text{BaZr}_{0.4}\text{Ce}_{0.4}\text{Y}_{0.2}\text{O}_{3-\delta}$	$\text{Ni-BaZr}_{0.4}\text{Ce}_{0.4}\text{Y}_{0.2}\text{O}_{3-\delta}$	~155	~170	⁴
$\text{Ba}_{0.5}\text{Sr}_{0.5}\text{Co}_{0.8}\text{Fe}_{0.2}\text{O}_{3-\delta}$	$\text{BaZr}_{0.8}\text{Y}_{0.2}\text{O}_{3-\delta}$	$\text{Ni-BaZr}_{0.8}\text{Y}_{0.2}\text{O}_{3-\delta}$	~23	~32	⁴
$\text{Pr}_2\text{NiO}_{4+\delta}$	$\text{BaZr}_{0.4}\text{Ce}_{0.4}\text{Y}_{0.2}\text{O}_{3-\delta}$	$\text{Ni-BaZr}_{0.85}\text{Y}_{0.15}\text{O}_{3-\delta}$	102	158	⁵
$\text{Ba}_{0.5}\text{Sr}_{0.5}(\text{Co}_{0.8}\text{Fe}_{0.2})_{0.9}\text{Ti}_{0.1}\text{O}_{3-\delta}-\text{BaZr}_{0.4}\text{Ce}_{0.4}\text{Y}_{0.2}\text{O}_{3-\delta}$	$\text{BaZr}_{0.4}\text{Ce}_{0.4}\text{Y}_{0.2}\text{O}_{3-\delta}$	$\text{Ni-BaZr}_{0.4}\text{Ce}_{0.4}\text{Y}_{0.2}\text{O}_{3-\delta}$	194	243	⁶
$\text{La}_{0.6}\text{Sr}_{0.4}\text{Co}_{0.2}\text{Fe}_{0.8}\text{O}_{3-\delta}$	$\text{BaZr}_{0.4}\text{Ce}_{0.4}\text{Y}_{0.2}\text{O}_{3-\delta}$	$\text{Ni-BaZr}_{0.4}\text{Ce}_{0.4}\text{Y}_{0.2}\text{O}_{3-\delta}$	279	340	⁷
$\text{La}_{0.6}\text{Sr}_{0.4}\text{Co}_{0.2}\text{Fe}_{0.8}\text{O}_{3-\delta}$	$\text{BaZr}_{0.6}\text{Ce}_{0.2}\text{Y}_{0.2}\text{O}_{3-\delta}$	$\text{Ni-BaZr}_{0.6}\text{Ce}_{0.2}\text{Y}_{0.2}\text{O}_{3-\delta}$	336	396	⁷
$\text{La}_{0.6}\text{Sr}_{0.4}\text{Co}_{0.2}\text{Fe}_{0.8}\text{O}_{3-\delta}$	$\text{BaZr}_{0.7}\text{Ce}_{0.1}\text{Y}_{0.2}\text{O}_{3-\delta}$	$\text{Ni-BaZr}_{0.7}\text{Ce}_{0.1}\text{Y}_{0.2}\text{O}_{3-\delta}$	111		⁷
$\text{La}_{0.6}\text{Sr}_{0.4}\text{Co}_{0.2}\text{Fe}_{0.8}\text{O}_{3-\delta}$	$\text{BaZr}_{0.8}\text{Y}_{0.2}\text{O}_{3-\delta}$	$\text{Ni-BaZr}_{0.8}\text{Y}_{0.2}\text{O}_{3-\delta}$	102		⁷
$\text{Sm}_{0.5}\text{Sr}_{0.5}\text{Co}_{0.3-\delta}\text{Ce}_{0.8}\text{Sm}_{0.2}\text{O}_{3-\delta}$	$\text{BaZr}_{0.8}\text{Y}_{0.2}\text{O}_{3-\delta}$	$\text{Ni-BaZr}_{0.1}\text{Ce}_{0.7}\text{Y}_{0.2}\text{O}_{3-\delta}$	55	70	⁸
$\text{La}_{0.6}\text{Sr}_{0.4}\text{Co}_{0.2}\text{Fe}_{0.8}\text{O}_{3-\delta}-\text{BaCe}_{0.7}\text{Zr}_{0.15}\text{Y}_{0.15}\text{O}_{3-\delta}$	$\text{BaCe}_{0.7}\text{Zr}_{0.15}\text{Y}_{0.15}\text{O}_{3-\delta}$	$\text{Ni-BaCe}_{0.7}\text{Zr}_{0.15}\text{Y}_{0.15}\text{O}_{3-\delta}$	~190	~260	⁹
$\text{BaZr}_{0.1}\text{Ce}_{0.7}\text{Y}_{0.2}\text{O}_{3-\delta}-\text{Sm}_{0.5}\text{Sr}_{0.5}\text{CoO}_{3-\delta}$	$\text{BaZr}_{0.1}\text{Ce}_{0.7}\text{Y}_{0.2}\text{O}_{3-\delta}$	$\text{Ni-BaZr}_{0.1}\text{Ce}_{0.7}\text{Y}_{0.2}\text{O}_{3-\delta}$	445	598	¹⁰

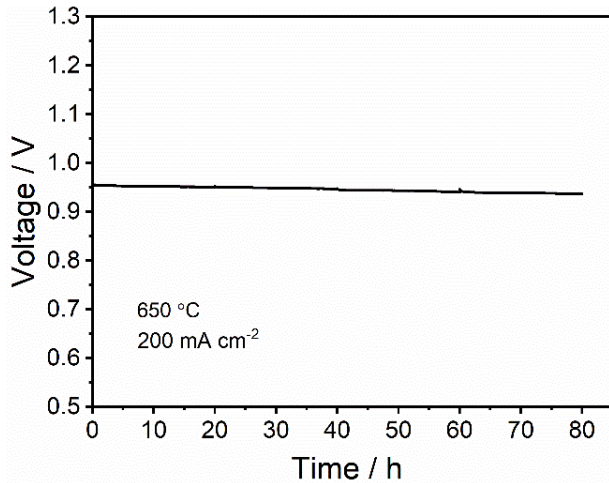


Figure S2. Durability test of the PCC cell at 200 mA cm^{-2} and $650 \text{ }^{\circ}\text{C}$ in fuel cell mode with wet hydrogen on the fuel electrode side and wet air on the oxygen electrode side.

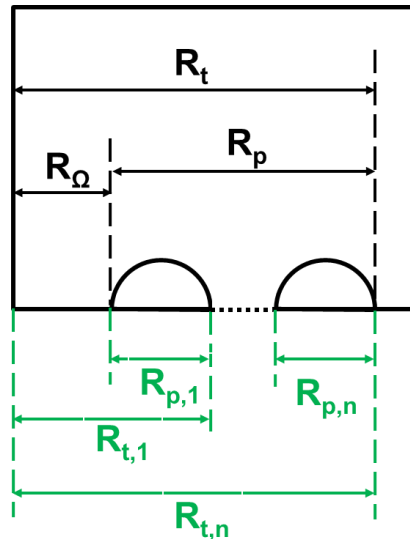


Figure S3. Simulated Nyquist plot of impedance spectra for the circuit containing n $(\text{RQ})_i$ elements.

Note S1

Typically, in Nyquist plots (Figure S3) of SOCs with YSZ electrolyte which is a pure oxygen ion conductor, the first x -axis intercept at the high frequency regime could be considered as ohmic resistance (R_Ω), which normally arises from the bulk resistance in electrolyte, while the intercept of the squashed arcs in between corresponds to the polarization resistance (R_p), which is related with the electrochemical reaction in both fuel electrode and oxygen electrode. In PCC cells, however, the existence of electronic conduction through the electrolyte makes the real polarization resistance ($R_{p,r}$) different from the apparent polarization resistance (R_p). Therefore,

the electronic resistance (R_e) was introduced parallelly into the equivalent circuit shown in Figure 3a. At the high frequency intercept, the polarization capacitance could be assumed to be short-circuited. Hence, R_Ω representing the apparent ohmic resistance is given as

$$R_\Omega = \frac{R_e R_i}{R_e + R_i} , \quad (1)$$

where R_e and R_i indicate electronic resistance and ionic resistance in the electrolyte. At lower frequencies, the polarization resistance contributes to the impedance and the total resistance (R_t) can be expressed as

$$R_t = \frac{R_e(R_i + R_{p,r})}{R_e + (R_i + R_{p,r})} , \quad (2)$$

where $R_{p,r}$ represents the real polarization resistance under the influence of electronic conduction through electrolyte. Since R_e can be expressed as

$$R_e = \frac{R_t}{1 - \frac{V_{OC}}{V_N}} , \quad (3)$$

where V_{OC} and V_N are the measured open circuit voltage and computed Nernst voltage, respectively.¹¹ Consequently, the average ionic transference number (t_i) and R_i can be expressed and calculated by

$$t_i = \frac{R_e}{R_e + R_i} = 1 - \frac{R_\Omega}{R_t} \left(1 - \frac{V_{OC}}{V_N}\right) , \quad (4)$$

$$R_i = \frac{R_\Omega}{t_i} . \quad (5)$$

Substitution of equation (3) and (4) into (2), the real polarization resistance can be calculated based on R_t , R_Ω and t_i , as expressed below

$$R_{p,r} = \frac{R_\Omega(R_t - R_\Omega)}{t_i[R_t - (R_t - R_\Omega)]} . \quad (6)$$

In practical resistance analysis, there will be more than one RQ element required in the equivalent circuit based on the physico-chemical processes as shown in Figure 3b. The real polarization resistance ($R_{p,r,i}$) for each $(RQ)_i$ element can be calculated as well by using equation (6).

Table S2. Electrochemical characteristics of representative PCC cells at OCV in fuel cell mode.

T	R _t	R _Ω	R _p	R _{p,r}	R _i	R _e	t _i	t _e
°C	Ω cm ²							
500	2.460	0.823	1.637	1.673	0.827	153.999	0.995	0.005
550	1.131	0.569	0.562	0.585	0.577	42.021	0.986	0.014
600	0.615	0.421	0.194	0.209	0.434	14.589	0.971	0.029
650	0.397	0.322	0.075	0.085	0.340	6.092	0.947	0.053
700	0.287	0.250	0.037	0.045	0.273	3.014	0.917	0.083

Table S3. Comparison of the PCFC with BGLC587-BZCY541 oxygen electrode at 600 °C in this study with the best performance PCFCs using different proton conducting electrolytes.

Air electrode	Electrolyte	Fuel electrode	PPD	R _Ω	R _p	Ref.
BGLC587-BZCY541	BaZr _{0.5} Ce _{0.4} Y _{0.1} O _{3-δ} ~12 μm	Ni-BaZr _{0.5} Ce _{0.4} Y _{0.1} O _{3-δ}	403	0.421	0.194	This work
NBSCF	BaZr _{0.1} Ce _{0.7} Y _{0.1} Yb _{0.1} O _{3-δ} ~15 μm	Ni-BaZr _{0.1} Ce _{0.7} Y _{0.1} Yb _{0.1} O _{3-δ}	690	0.128	0.283	¹²
PBCC	BaZr _{0.1} Ce _{0.7} Y _{0.1} Yb _{0.1} O _{3-δ} ~10 μm	Ni-BaZr _{0.1} Ce _{0.7} Y _{0.1} Yb _{0.1} O _{3-δ}	1060	~0.1	~0.2	¹³
PBCFN	BaZr _{0.1} Ce _{0.7} Y _{0.1} Yb _{0.1} O _{3-δ} ~10 μm	Ni-BaZr _{0.1} Ce _{0.7} Y _{0.1} Yb _{0.1} O _{3-δ}	723	~0.15	~0.28	¹⁴
BSCF	BaCe _{0.55} Zr _{0.3} Y _{0.15} O _{3-δ} 5 μm	Ni-BaCe _{0.55} Zr _{0.3} Y _{0.15} O _{3-δ}	1302	0.09	0.09	¹⁵
LSC (Pulsed laser deposition)	BaZr _{0.85} Y _{0.15} O _{3-δ} ~2 μm (Pulsed laser deposition)	Ni-BaZr _{0.85} Y _{0.15} O _{3-δ}	740	~0.1	~0.15	¹⁶
LSC (Pulsed laser deposition)	BaCe _{0.55} Zr _{0.3} Y _{0.15} O _{3-δ} ~1 μm (Pulsed laser deposition)	Ni-BaCe _{0.55} Zr _{0.3} Y _{0.15} O _{3-δ} (Pulsed laser deposition)	1100	~0.06	~0.23	¹⁷

NBSCF=NdBa_{0.5}Sr_{0.5}Co_{1.5}Fe_{0.5}O_{5+δ};PBCC= PrBa_{0.8}Ca_{0.2}Co₂O_{5+δ};PBCFN= PrBaCo_{1.6}Fe_{0.2}Nb_{0.2}O_{5+δ};BSCF= Ba_{0.5}Sr_{0.5}Co_{0.8}Fe_{0.2}O_{3-δ};LSC=La_{0.6}Sr_{0.4}CoO_{3-δ};

Note S2

Table S3 summarizes some of the best PCFC performances published in recent years. The relatively high ohmic losses of our BZCY541 electrolyte could be explained by the Zr-rich phase of the material compared to those of the other cells in this table. However, the low polarization resistance is still competitive.

Table S4. Comparison of the PCC cell with BGLC587-BZCY541 oxygen electrode in steam electrolysis mode at 600 °C with PCC cells from previous studies.

Air electrode	Electrolyte	Fuel electrode	Air electrode gas composition	Current density at 1.3 V (A cm ⁻²)	Ref.
BGLC587-BZCY541	BZCY541	Ni-BZCY541	Air (30% H ₂ O)	-0.650	This work
La _{0.6} Sr _{0.4} Co _{0.2} Fe _{0.8} O _{3-δ} -BaZr _{0.8} Y _{0.2} O _{3-δ}	BaZr _{0.8} Y _{0.2} O _{3-δ}	Ni-BaZr _{0.8} Y _{0.2} O _{3-δ}	Air (3% H ₂ O)	-0.053	¹⁸
Sm _{0.5} Sr _{0.5} CoO _{3-δ} -BaCe _{0.5} Zr _{0.3} Y _{0.2} O _{3-δ}	BaCe _{0.5} Zr _{0.3} Y _{0.2} O _{3-δ}	Ni-BaCe _{0.5} Zr _{0.3} Y _{0.2} O _{3-δ}	Air (50% H ₂ O)	-0.190	¹⁹
Sr ₂ Fe _{1.5} Mn _{0.5} O _{6-δ} -BaZr _{0.8} Y _{0.2} O _{3-δ}	BaZr _{0.8} Y _{0.2} O _{3-δ}	Ni-BaZr _{0.8} Y _{0.2} O _{3-δ}	Air (3% H ₂ O)	-0.210	²⁰
Pr ₂ NiO _{4+δ} -BaZr _{0.2} Ce _{0.6} Y _{0.2} O _{3-δ}	BaZr _{0.2} Ce _{0.6} Y _{0.2} O _{3-δ}	Ni-BaZr _{0.2} Ce _{0.6} Y _{0.2} O _{3-δ}	Air (40% H ₂ O)	-0.600	²¹
SrEu ₂ Fe _{1.8} Coo _{0.2} O _{7-δ} -BaZr _{0.5} Ce _{0.3} Y _{0.2} O _{3-δ}	BaZr _{0.5} Ce _{0.3} Y _{0.2} O _{3-δ}	Ni-BaZr _{0.5} Ce _{0.3} Y _{0.2} O _{3-δ}	Air (10% H ₂ O)	-0.350	²²
Sr _{2.8} La _{0.2} Fe ₂ O _{7-δ}	BaCe _{0.5} Zr _{0.3} Y _{0.2} O _{3-δ}	Ni-BaCe _{0.5} Zr _{0.3} Y _{0.2} O _{3-δ}	Air (20% H ₂ O)	-0.460	²³
La _{1.2} Sr _{0.8} NiO ₄	BaCe _{0.7} Zr _{0.1} Y _{0.2} O _{3-δ}	Ni-BaCe _{0.7} Zr _{0.1} Y _{0.2} O _{3-δ}	Air (20% H ₂ O)	-0.420	²⁴
Pr _{1.2} Sr _{0.8} NiO ₄	BaCe _{0.7} Zr _{0.1} Y _{0.2} O _{3-δ}	Ni-BaCe _{0.7} Zr _{0.1} Y _{0.2} O _{3-δ}	Air (20% H ₂ O)	-0.350	²⁴
(PrBa _{0.8} Ca _{0.2}) _{0.95} Co ₂ O _{6-δ}	BaCe _{0.4} Zr _{0.4} Y _{0.1} Yb _{0.1} O _{3-δ}	Ni-BaCe _{0.4} Zr _{0.4} Y _{0.1} Yb _{0.1} O _{3-δ}	O ₂ (20% H ₂ O)	-0.720	²⁵
PrBa _{0.8} Ca _{0.2} Co ₂ O _{6-δ}	BaCe _{0.4} Zr _{0.4} Y _{0.1} Yb _{0.1} O _{3-δ}	Ni-BaCe _{0.4} Zr _{0.4} Y _{0.1} Yb _{0.1} O _{3-δ}	O ₂ (20% H ₂ O)	-0.505	²⁵

Table S5. Electrochemical characteristics of representative PCC cells at OCV in steam electrolysis operation.

T °C	R _t Ω cm ²	R _Ω Ω cm ²	R _p Ω cm ²	R _{p,r} Ω cm ²	R _i Ω cm ²	R _e Ω cm ²	t _i	t _e
500	3.117	0.975	2.142	2.196	0.980	166.678	0.994	0.006
550	1.554	0.617	0.937	0.965	0.622	73.926	0.992	0.008
600	0.809	0.464	0.345	0.362	0.473	26.481	0.982	0.018
650	0.514	0.355	0.159	0.170	0.365	13.053	0.973	0.027
700	0.385	0.279	0.106	0.118	0.292	6.397	0.956	0.044

Table S6. Electrochemical characteristics of representative PCC cells at OCV in steam electrolysis operation at different steam concentrations mixed with air on the oxygen electrode side.

pH ₂ O atm	V _{OC} V	V _E V	R _t Ω cm ²	R _Ω Ω cm ²	R _p Ω cm ²	R _{p,r} Ω cm ²	R _i Ω cm ²	R _e Ω cm ²	t _i	t _e
0.05	0.998	1.055	0.744	0.437	0.308	0.335	0.451	13.918	0.969	0.031
0.1	0.982	1.028	0.778	0.430	0.348	0.374	0.440	17.334	0.975	0.025
0.3	0.954	0.982	0.832	0.422	0.410	0.427	0.428	29.986	0.986	0.014
0.5	0.930	0.956	0.860	0.422	0.438	0.456	0.428	31.621	0.987	0.013
0.7	0.914	0.934	0.905	0.418	0.487	0.502	0.422	42.410	0.990	0.010

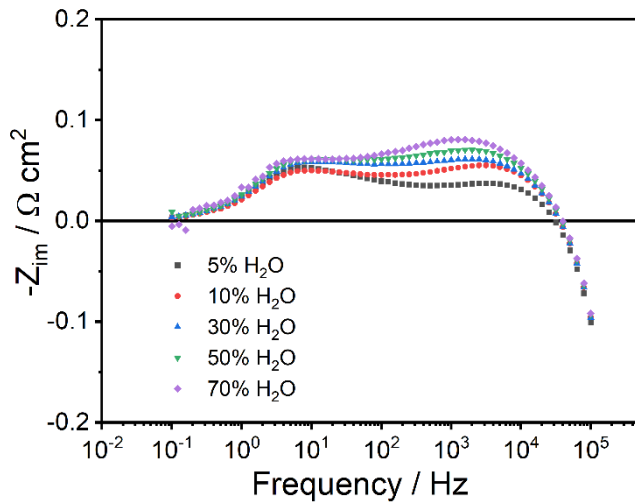


Figure S4. Imaginary impedance spectra of the cell measured with various H_2O concentrations (5–70%) mixed with air at OCV.

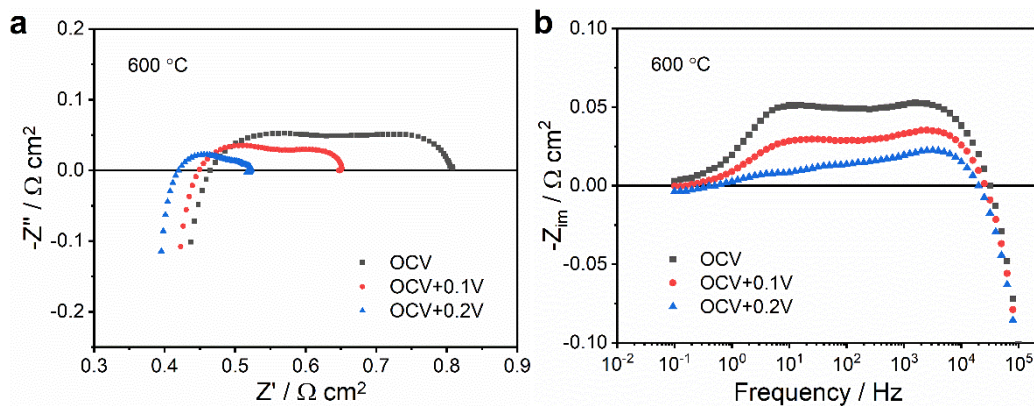


Figure S5. Electrochemical impedance spectra of the PCC cell with BGLC587-BZCY541 oxygen electrode measured at various electrolysis voltages with humidified 20% H_2 -80% N_2 and 30% H_2O -70% air supplied to the fuel and oxygen electrode, respectively.

Table S7. Analysis of the impedance spectra at various electrolysis voltages for steam electrolysis at 600 °C.

Voltage	R_t	R_Ω	R_p	$R_{p,r}$	R_i	R_e	t_i	t_e
V	$\Omega \text{ cm}^2$							
OCV	0.809	0.464	0.345	0.362	0.473	26.481	0.982	0.018
OCV+0.1	0.650	0.449	0.201	0.228	0.473	8.959	0.950	0.050
OCV+0.2	0.522	0.420	0.102	0.133	0.473	3.768	0.889	0.111

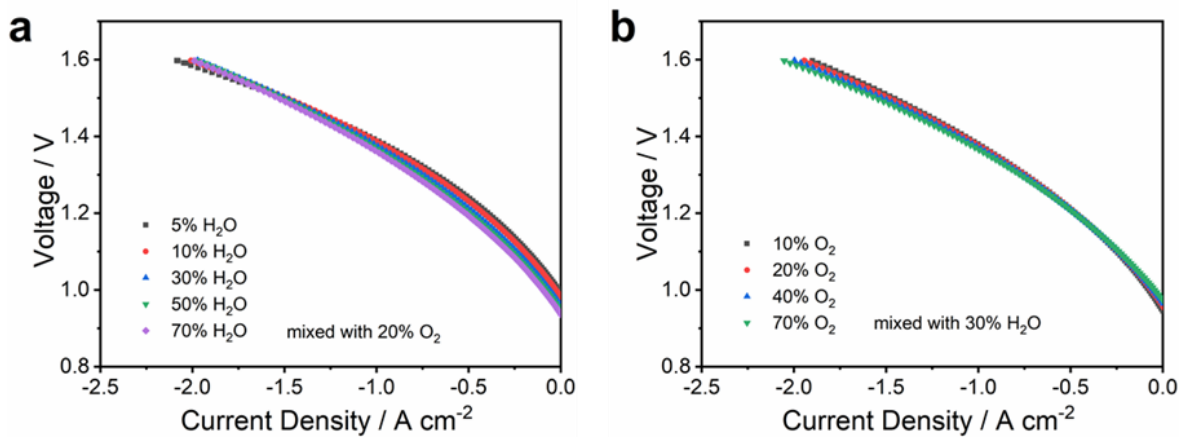


Figure S6. Gaseous atmosphere dependence of I-V curves of BGLC587-BZCY541 oxygen electrode cells at 600 °C. I-V curves as a function of H₂O partial pressure ($p_{\text{H}_2\text{O}}$) (a) and O₂ partial pressure (p_{O_2}) (b). The mixed gas was balanced with N₂ on the oxygen electrode side.

Table S8. Composition of high-performance PCECs and their faradaic efficiency determined by gas analysis in steam electrolysis operation.

Cell configuration:	Gas composition		Current density at 1.3 V (A cm ⁻²)	η_{FE} at voltages or current densities	Ref.
Air electrode	Oxygen electrode	Fuel electrode			
Air electrode					
BZCY541	70%H ₂ O/Air	20%H ₂ /N ₂ (3%H ₂ O)	-0.70 (600 °C)	68% at -0.8 A cm ⁻² 75% at -0.4 A cm ⁻² (600 °C)	This work
Ni-BZCY541					
BZCY541	30%H ₂ O/Air	20%H ₂ /N ₂ (3%H ₂ O)	-0.71 (600 °C)	60% at -0.8 A cm ⁻² 70% at -0.4 A cm ⁻² (600 °C)	This work
Ni-BZCY541					
PBSCF	3%H ₂ O/Air	5%H ₂ /Ar	-1.30 (600 °C)	~48% at -1.3 A cm ⁻² (600 °C)	²⁶
BZCYYb4411					
Ni-BZCYYb4411					
PBCFN	3%H ₂ O/Air	3%H ₂ O/H ₂	-2.15 (650 °C)	~43% at -1.0 A cm ⁻² (650 °C)	¹⁴
BZCYYb1711					
Ni-BZCYYb1711					
PBCC	30%H ₂ O/Air	3%H ₂ O/H ₂	-1.351 (600 °C)	~83% at 1.3 V (600 °C)	¹³
BZCYYb1711					
Ni-BZCYYb1711					
SLF	20%H ₂ O/Air	3%H ₂ O/H ₂	-1.08 (700 °C)	~25% at -0.3 A cm ⁻² (700 °C)	²³
BZCY352					
Ni-BZCY352					
SLF	20%H ₂ O/Air	3%H ₂ O/H ₂	-0.46 (600 °C)	-	²³
BZCY352					
Ni-BZCY352					
PNC	15%H ₂ O/Air	5%H ₂ /Ar	-0.81 (600 °C)	~80% at 1.3 V (600 °C)	²⁷
BZCYYb4411					
Ni-BZCYYb4411					
BCFZY-BZCYYb4411	10%H ₂ O/Air	H ₂	-	~75% at -0.5 A cm ⁻² (550 °C)	²⁸
BZCYYb4411					
Ni-BZCYYb4411					
BCFZY-BZCYYb1711	20%H ₂ O/O ₂ -N ₂	Ar	-1.10 (600 °C)	~99% at -1.1 A cm ⁻² (600 °C)	²⁹
BZCYYb1711					
Ni-BZCYYb1711					
BCFZY-BZCYYb1711	10%H ₂ O/O ₂ -N ₂	Ar	-1.10 (600 °C)	~85% at -1.1 A cm ⁻² (600 °C)	²⁹
BZCYYb1711					
Ni-BZCYYb1711					
BCFZY-BZY20	20%H ₂ O/O ₂ -N ₂	Ar	-0.90 (600 °C)	~50% at -0.9 A cm ⁻² (600 °C)	²⁹
BZY20					
Ni-BZY20					

PBSCF= PrBa_{0.5}Sr_{0.5}Co_{1.5}Fe_{0.5}O_{5+δ}; PBCFN= PrBaCo_{1.6}Fe_{0.2}Nb_{0.2}O_{5+δ}; PBCC=PrBa_{0.8}Ca_{0.2}Co₂O_{5+δ}; SLF= Sr_{2.8}La_{0.2}Fe₂O_{7-δ}

PNC= PrNi_{0.5}Coo_{0.5}O_{3-δ}; BCFZY= BaCoo_{0.4}Fe_{0.4}Zr_{0.1}Y_{0.1}O_{3-δ}; BZCYYb4411= BaZr_{0.4}Ce_{0.4}Y_{0.1}Yb_{0.1}O_{3-δ}; BZCYY1711=BaZr_{0.1}Ce_{0.7}Y_{0.1}Yb_{0.1}O_{3-δ}; BZCY352= BaZr_{0.3}Ce_{0.5}Y_{0.2}O_{3-δ}; BZY20=BaZr_{0.8}Ce_{0.2}O_{3-δ}

Note S3.

High-temperature solid oxide electrolyzers based on oxygen ion conductors can reach electrical efficiency of 100% at thermoneutral voltage, that is ca. 1.3 V, which corresponds to practical use cases of the technology for industrial hydrogen production. Table S8 summarizes some of the high-performance fuel electrode supported PCEC in steam electrolysis operation and their faradaic efficiency determined at ~1.3 V. Some of the current density values at 1.3 V listed in Table S8 were estimated based on the polarization curves from the given references. The faradaic efficiency measured at voltages far below 1.3V or at comparatively low current densities (less than 400 A cm⁻²) in literature was excluded in the Table S8, due to the lack of significance for practical usage of the technology. The faradaic efficiency value was comparatively low and demonstrated that more than 50% of the applied current was lost by the electronic leakage. This is detrimental for the energy conversion efficiency. Therefore, it is crucial for the development of high-performance PCEC to achieve high faradaic efficiency values at high current densities of ~1.3 V.

Note S4. DRT analysis

To elucidate the reaction kinetics in the oxygen electrode for steam electrolysis, the distribution of relaxation times (DRT) analysis and equivalent circuit model (ECM) fitting were performed based on the electrochemical impedance of the full cells with BGLC587-BZCY541 oxygen electrodes. The different impedance spectra were recorded with the variation of *pH₂O* and *pO₂*, accordingly, on the oxygen electrode side. To identify the specific contributions from the relevant processes to the impedance spectra, gas partial pressure variations can help. For example, when EIS measurements are compared where only *pH₂O* or *pO₂* were changed, the differences in the spectra should be related to the changes on the oxygen electrode side. Furthermore, the change of *R_p* with *pH₂O* or *pO₂* can give mechanistic insights into the nature of rate-limiting elementary kinetic step. If a single elementary reaction is the rate determining step, the dependence of the separated process in the impedance on *pH₂O* and *pO₂* should allow for its assignment to an elementary step based on a comparison with the kinetics formulated by the law of mass action.

Table S9. Electrochemical characteristics of representative PCC cells under OCV condition in steam electrolysis operation with various $p\text{H}_2\text{O}$ and $p\text{O}_2$ on oxygen electrode side.

$p\text{H}_2\text{O}$	$p\text{O}_2$	V_{OC}	V_{E}	R_t	R_Ω	R_p	$R_{p,r}$	R_i	R_e	t_i	t_e
atm	atm	V	V	$\Omega \text{ cm}^2$							
0.05	0.2	1.000	1.055	0.701	0.407	0.294	0.320	0.420	13.450	0.970	0.030
0.1	0.2	0.989	1.029	0.707	0.399	0.308	0.327	0.408	18.186	0.978	0.022
0.3	0.2	0.967	0.987	0.722	0.394	0.327	0.338	0.399	35.614	0.989	0.011
0.5	0.2	0.953	0.968	0.736	0.383	0.353	0.362	0.386	47.528	0.992	0.008
0.3	0.1	0.953	0.974	0.801	0.402	0.399	0.412	0.406	37.141	0.989	0.011
0.3	0.2	0.965	0.987	0.728	0.392	0.335	0.347	0.397	32.639	0.988	0.012
0.3	0.4	0.976	1.000	0.668	0.385	0.282	0.293	0.391	27.825	0.986	0.014
0.3	0.7	0.984	1.011	0.626	0.376	0.250	0.261	0.383	23.443	0.984	0.016



Figure S7. The equivalent circuit model proposed with the fitting on impedance spectra of PH_2O and PO_2 variations in oxygen electrode.

Note S5.

The curved lines of the Nyquist plots (Figure 5a and 5b) in the high-frequency region indicate the influence of parasitic inductance in the test rig.³⁰ The typical values of L are $10^{-7}\text{--}10^{-6}$ H. A practical way to eliminate such influences is to use low-inductance cables by twisting the wires between the test rig and measurement device. In our study, due to the fixed configuration of the commercial test rig, twisting the wires is only possible to a limited extent. In order to model the effect from inductance, the introduction of an inductance element to the fitting model is indispensable.

Table S10. Fitting data of the impedance spectra with variation of $p\text{H}_2\text{O}$ (a) and $p\text{O}_2$ (b) at OCV and the temperature of 600 °C.

	H ₂ O dependence / atm ($p\text{O}_2 = 0.20P_0$)				O ₂ dependence / atm ($p\text{H}_2\text{O} = 0.30P_0$)			
	0.05	0.1	0.3	0.5	0.1	0.2	0.4	0.7
R1 / $\Omega \text{ cm}^2$	0.064	0.066	0.067	0.069	0.094	0.086	0.091	0.084
C1 / F cm^{-2}	1.1×10^{-4}	8.9×10^{-5}	9.3×10^{-5}	6.9×10^{-5}	7.9×10^{-5}	7.3×10^{-5}	7.3×10^{-5}	7.2×10^{-5}
R2 / $\Omega \text{ cm}^2$	0.061	0.076	0.100	0.126	0.120	0.100	0.073	0.061
C2 / F cm^{-2}	7.1×10^{-4}	6.2×10^{-4}	5.8×10^{-4}	4.5×10^{-4}	6.3×10^{-4}	6.3×10^{-4}	9.8×10^{-4}	9.5×10^{-4}
R3 / $\Omega \text{ cm}^2$	0.058	0.057	0.058	0.060	0.070	0.059	0.046	0.035
C3 / F cm^{-2}	1.7×10^{-2}	1.6×10^{-2}	1.7×10^{-2}	1.7×10^{-2}	2.1×10^{-2}	2.0×10^{-2}	3.2×10^{-2}	3.0×10^{-2}
R4 / $\Omega \text{ cm}^2$	0.111	0.109	0.103	0.100	0.115	0.090	0.073	0.070
C4 / F cm^{-2}	2.4×10^{-1}	2.3×10^{-1}	2.4×10^{-1}	2.4×10^{-1}	2.4×10^{-1}	2.9×10^{-1}	4.1×10^{-1}	4.5×10^{-1}

Table S11. Polarization resistances of the PCC cells with BGLC587-BZCY541 oxygen electrode at OCV and various $p\text{H}_2\text{O}$ and $p\text{O}_2$ on the oxygen electrode side.

$p\text{H}_2\text{O}$	$p\text{O}_2$	$R_{p,1}$	$R_{p,2}$	$R_{p,3}$	$R_{p,4}$	$R_{p,r,1}$	$R_{p,r,2}$	$R_{p,r,3}$	$R_{p,r,4}$
atm	atm	$\Omega \text{ cm}^2$							
0.05	0.2	0.064	0.061	0.058	0.111	0.068	0.066	0.063	0.123
0.1	0.2	0.066	0.076	0.057	0.109	0.069	0.080	0.061	0.117
0.3	0.2	0.067	0.100	0.058	0.103	0.069	0.103	0.060	0.107
0.5	0.2	0.069	0.126	0.060	0.099	0.070	0.129	0.061	0.102
0.3	0.1	0.094	0.120	0.070	0.115	0.096	0.123	0.073	0.120
0.3	0.2	0.086	0.100	0.059	0.090	0.089	0.103	0.061	0.094
0.3	0.4	0.091	0.073	0.046	0.073	0.094	0.076	0.048	0.076
0.3	0.7	0.084	0.061	0.035	0.070	0.087	0.064	0.036	0.073

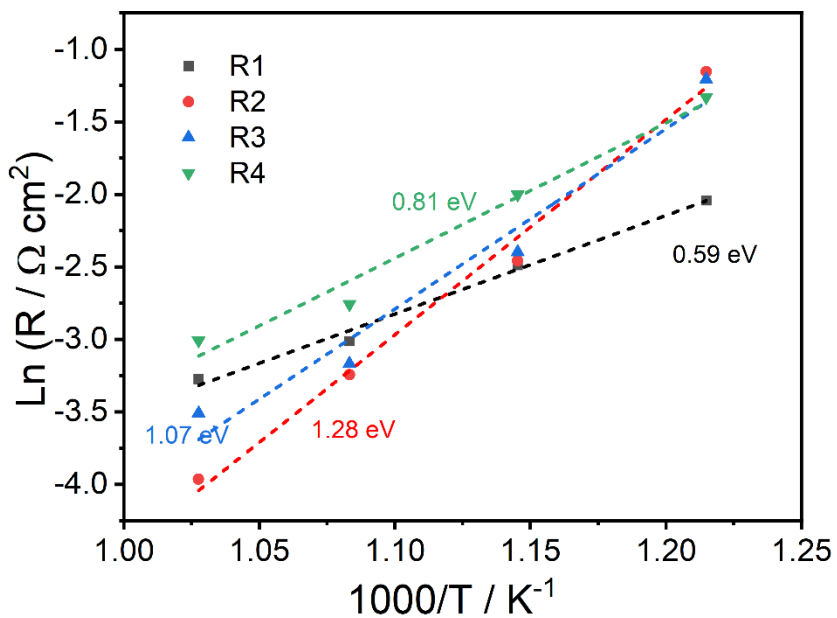


Figure S8. Arrhenius plot of different resistances (R_1 , R_2 , R_3 and R_4) derived from impedance spectra and the corresponding activation energy with (wet) 20% H_2 -80% N_2 on the fuel electrode side and 30% H_2O -70% air on the oxygen electrode side.

Table S12. Reaction models for elementary reaction steps at oxygen electrode for water splitting in proton conducting ceramic cells.

Step	Elementary reactions
Step 1	$H_2O(g) \rightarrow H_2O(\text{ads})$
Step 2	$H_2O(\text{ads}) \rightarrow O^{2-}(\text{ads}) + 2H^+(\text{surface, electrode})$
Step 3	$H^+(\text{surface, electrode}) \rightarrow H^+(\text{interface, electrode})$
Step 4	$H^+(\text{interface, electrode}) \rightarrow H^+(\text{electrolyte})$
Step 5	$O^{2-}(\text{ads}) \rightarrow O^-(\text{ads}) + e^-$
Step 6	$2O^-(\text{ads}) \rightarrow O_2^{2-}(\text{ads})$
Step 7	$O_2^{2-}(\text{ads}) \rightarrow O_2(\text{ads}) + 2e^-$
Step 8	$O_2(\text{ads}) \rightarrow O_2(g)$

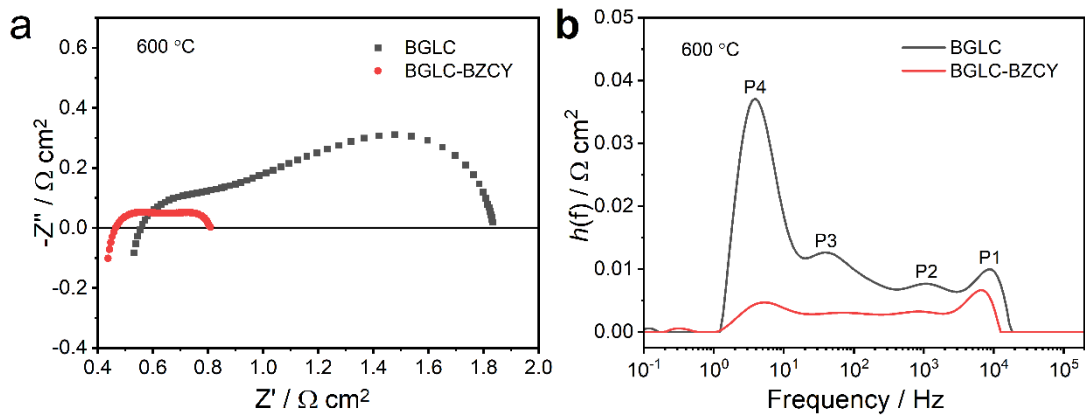


Figure S9. Nyquist impedance plot (a) and DRT deconvolution results (b) of PCCs with BGLC oxygen electrode and BGLC-BZCY composite oxygen electrode at OCV and 600 °C with (wet) 20% H₂-80% N₂ on the fuel electrode side and 30% H₂O-70% air on the oxygen electrode side.

Table S13. Fitting data of the impedance spectra of PCCs with BGLC oxygen electrode and BGLC-BZCY composite oxygen electrode at OCV and 600 °C with (wet) 20% H₂-80% N₂ on the fuel electrode side and 30% H₂O-70% Air on the oxygen electrode side.

Oxygen electrode	R1 $\Omega \text{ cm}^2$	C1 $F \text{ cm}^{-2}$	R2 $\Omega \text{ cm}^2$	C2 $F \text{ cm}^{-2}$	R3 $\Omega \text{ cm}^2$	C3 $F \text{ cm}^{-2}$	R4 $\Omega \text{ cm}^2$	C4 $F \text{ cm}^{-2}$
BGLC	0.168	7.2×10^{-5}	0.248	8.3×10^{-4}	0.440	9.9×10^{-2}	0.461	1.4×10^{-2}
BGLC-BZCY	0.080	9.7×10^{-5}	0.082	8.1×10^{-4}	0.087	1.0×10^{-2}	0.128	1.5×10^{-1}

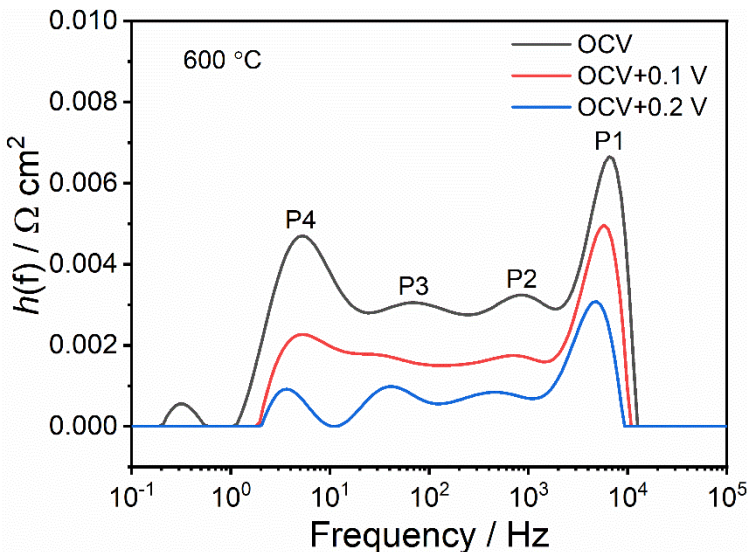


Figure S10. DRT deconvolution results of PCCs with BGLC-BZCY composite oxygen electrode at different voltages (OCV, OCV + 0.1 V and OCV + 0.2 V) and 600 °C with (wet) 20% H₂-80% N₂ on fuel electrode side and 30% H₂O-70% Air on oxygen electrode side.

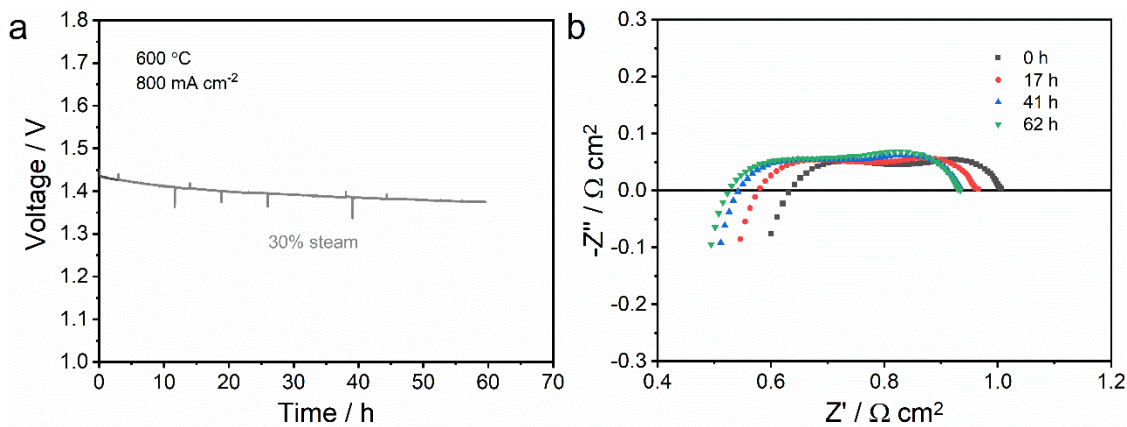


Figure S11. (a) Long-term stability of voltage evolution at 600 °C and a fixed current density of -0.8 A cm^{-2} with 20% H₂ mixed with 80% N₂ in fuel electrode and 30% H₂O mixed air in the oxygen electrode. (b) Electrochemical impedance spectroscopy of the cell before and after 62 h operation.

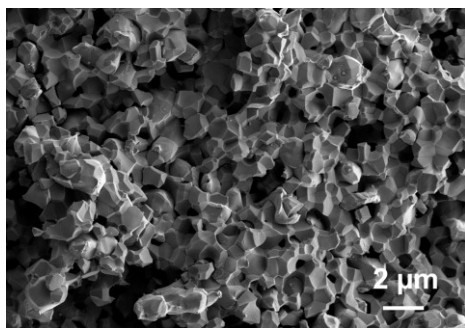


Figure S12. SEM cross-section of the fuel electrode after 366 h operation for steam electrolysis.

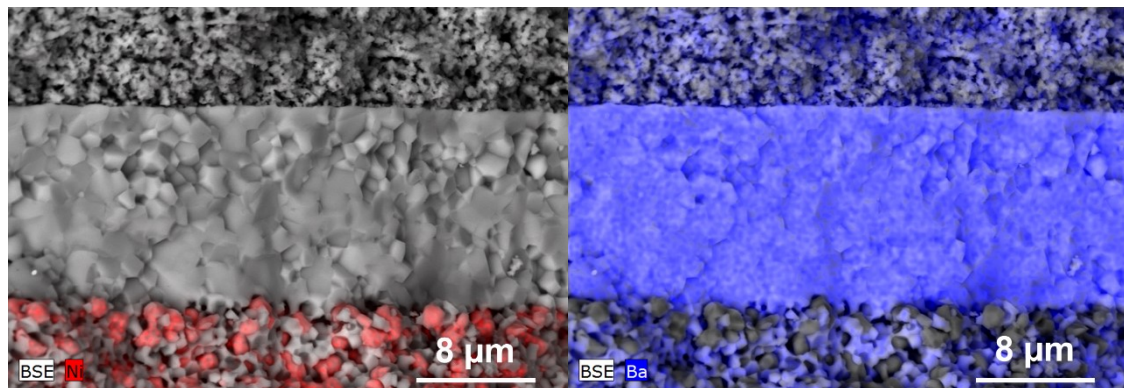


Figure S13. EDX elemental mapping of the cell after 366 h operation for steam electrolysis.

References

1. L. Fan and P.-C. Su, *J. Power Sources*, 2016, **306**, 369-377.
2. A. Zhu, G. Zhang, T. Wan, T. Shi, H. Wang, M. Wu, C. Wang, S. Huang, Y. Guo and H. Yu, *Electrochim. Acta*, 2018, **259**, 559-565.
3. F. Zhao, S. Wang, K. Brinkman and F. Chen, *J. Power Sources*, 2010, **195**, 5468-5473.
4. Y. Guo, Y. Lin, R. Ran and Z. Shao, *J. Power Sources*, 2009, **193**, 400-407.
5. N. Nasani, D. Ramasamy, S. Mikhalev, A. V. Kovalevsky and D. P. Fagg, *J. Power Sources*, 2015, **278**, 582-589.
6. L. Bi, E. Fabbri and E. Traversa, *Electrochim. commun.*, 2012, **16**, 37-40.
7. S. Jeong, T. Kobayashi, K. Kuroda, H. Kwon, C. Zhu, H. Habazaki and Y. Aoki, *RSC adv.*, 2018, **8**, 26309-26317.
8. J. Xiao, W. Sun, Z. Zhu, Z. Tao and W. Liu, *Mater. Lett.*, 2012, **73**, 198-201.
9. H. Lee, S. Lee, T. Lee, S. Park and D. Shin, *Int. J. Hydrog. Energy*, 2017, **42**, 3748-3752.
10. L. Yang, C. Zuo, S. Wang, Z. Cheng and M. Liu, *Adv. Mater.*, 2008, **20**, 3280-3283.
11. M. Liu and h. Hu, *J. Electrochem. Soc.*, 1996, **143**, L109-L112.
12. J. Kim, S. Sengodan, G. Kwon, D. Ding, J. Shin, M. Liu and G. Kim, *ChemSusChem*, 2014, **7**, 2811-2815.
13. Y. Zhou, E. Liu, Y. Chen, Y. Liu, L. Zhang, W. Zhang, Z. Luo, N. Kane, B. Zhao, L. Soule, Y. Niu, Y. Ding, H. Ding, D. Ding and M. Liu, *ACS Energy Lett.*, 2021, **6**, 1511-1520.
14. K. Xu, H. Zhang, Y. Xu, F. He, Y. Zhou, Y. Pan, J. Ma, B. Zhao, W. Yuan, Y. Chen and M. Liu, *Adv. Funct. Mater.*, 2022, **32**, 2110998.

15. H. An, H.-W. Lee, B.-K. Kim, J.-W. Son, K. J. Yoon, H. Kim, D. Shin, H.-I. Ji and J.-H. Lee, *Nat Energy*, 2018, **3**, 870-875.
16. K. Bae, D. Y. Jang, H. J. Choi, D. Kim, J. Hong, B. K. Kim, J. H. Lee, J. W. Son and J. H. Shim, *Nat. Commun.*, 2017, **8**, 14553.
17. K. Bae, D. H. Kim, H. J. Choi, J.-W. Son and J. H. Shim, *Adv. Energy Mater.*, 2018, **8**, 1801315.
18. L. Bi, S. P. Shafi and E. Traversa, *J. Mater. Chem. A*, 2015, **3**, 5815-5819.
19. F. He, D. Song, R. Peng, G. Meng and S. Yang, *J. Power Sources*, 2010, **195**, 3359-3364.
20. L. Lei, Z. Tao, X. Wang, J. P. Lemmon and F. Chen, *J. Mater. Chem. A*, 2017, **5**, 22945-22951.
21. W. Y. Li, B. Guan, L. Ma, S. S. Hu, N. Zhang and X. B. Liu, *J. Mater. Chem. A*, 2018, **6**, 18057-18066.
22. D. Huan, N. Shi, L. Zhang, W. Tan, Y. Xie, W. Wang, C. Xia, R. Peng and Y. Lu, *ACS Appl. Mater. Interfaces*, 2018, **10**, 1761-1770.
23. D. Huan, W. Wang, Y. Xie, N. Shi, Y. Wan, C. Xia, R. Peng and Y. Lu, *J. Mater. Chem. A*, 2018, **6**, 18508-18517.
24. S. Yang, Y. Wen, J. Zhang, Y. Lu, X. Ye and Z. Wen, *Electrochim. Acta*, 2018, **267**, 269-277.
25. W. Tang, H. Ding, W. Bian, W. Wu, W. Li, X. Liu, J. Y. Gomez, C. Y. Regalado Vera, M. Zhou and D. Ding, *J. Mater. Chem. A*, 2020, **8**, 14600-14608.
26. S. Choi, T. C. Davenport and S. M. Haile, *Energy Environ. Sci.*, 2019, **12**, 206-215.
27. H. Ding, W. Wu, C. Jiang, Y. Ding, W. Bian, B. Hu, P. Singh, C. J. Orme, L. Wang, Y. Zhang and D. Ding, *Nat. Commun.*, 2020, **11**, 1907.
28. L. Q. Le, C. Meisel, C. H. Hernandez, J. Huang, Y. Kim, R. O'Hayre and N. P. Sullivan, *J. Power Sources*, 2022, **537**, 231356.
29. C. C. Duan, R. Kee, H. Y. Zhu, N. Sullivan, L. Z. Zhu, L. Z. Bian, D. Jennings and R. O'Hayre, *Nat Energy*, 2019, **4**, 230-240.
30. P. Caliandro, A. Nakajo, S. Diethelm and J. Van herle, *J. Power Sources*, 2019, **436**, 226838.